Journal of Zhejiang University-SCIENCE A (Applied Physics & Engineering)
ISSN 1673-565X (Print); ISSN 1862-1775 (Online)
www.zju.edu.cn/jzus; www.springerlink.com
E-mail: jzus@zju.edu.cn

Experimental study on the interfacial delamination in a thermal barrier coating system at elevated temperatures*

Peng-fei ZHAO, Fu-lin SHANG‡

(*Department of Engineering Mechanics, School of Aerospace, Xi'an Jiaotong University, Xi'an 710049, China*)

E-mail: zhaopengfei@stu.xjtu.edu.cn; shangfl@mail.xjtu.edu.cn

Received Apr. 16, 2010; Revision accepted July 5, 2010; Crosschecked Sept. 6, 2010

Abstract: The failure mode and adhesion of thermal barrier coating (TBC) 8YSZ (ZrO_2+8% (w/w) Y_2O_3) deposited on NiCoCrAlTaY bond coat by atmospheric plasma spraying were investigated. A grooved modified three-point bending specimen that can generate a single interface crack to facilitate the control of crack growth was adopted for testing, which was conducted at the ambient temperature of 100 °C. The morphology and composition of fractured surfaces were examined by means of a scanning electron microscopy (SEM) and an energy disperse spectroscopy (EDS). Images and spectrum show that cracks are initiated and propagated exclusively within YSZ layer adjacent to top/bond coat interface. The load-displacement curves obtained exhibit similar shapes that indicate two distinct stages in crack initiation and stable crack growth. Finite element analyses were performed to extract the adhesion strength of the TBCs. The delamination toughness of the plasma-sprayed 8YSZ coatings at 100 °C, in terms of critical strain energy release rate G_c, can be reliably obtained from an analytical solution.

Key words: Thermal barrier coating (TBC), Three-point bending test, Finite element analysis, Delamination toughness
doi:10.1631/jzus.A1000173 **Document code:** A **CLC number:** O34

1 Introduction

Thermal barrier coatings (TBCs) made from yttria-stabilized zirconia (YSZ), deposited by a plasma-spray approach, have attracted ever-increasing attention for aircraft and industrial gas-turbine applications because of their excellent wear resistance, corrosion resistance, and thermal insulation for engine components (Miller, 1987; 1997; Brindley, 1996). The advantage of ceramic TBCs is well recognized for causing a temperature reduction of 100–300 °C at the metal surface, thus improving the durability of metal component and enhancing engine performance. However, due to increased turbine inlet temperature, coating spallation can result in accelerated failure of the structural components. Consequently, an in-depth understanding of the degradation mechanisms and the development of durability prediction models have become major concerns in the research work on TBCs within the last decade (Evans *et al.*, 2001).

A typical TBC system is composed of an oxidation resistant metallic bond coat (BC) on the superalloy substrate and a thermal insulating ceramic top coat (TC) attached to the BC. Experience from aircraft engine applications has revealed that BC oxidation and resistance of the TBC delaminating from the substrate are critical factors in determining the coating lifetime. Some of the degradation modes which can limit the lifetime of a TBC are: (1) microcracks interconnecting near the interfacial imperfections between lamellas within the ceramic coating results in TBC spallation; (2) thermally grown oxide (TGO) formed along the TC/BC interface degrades the interfacial adhesion strength and toughness significantly. It has been shown that typical failure modes of plasma-sprayed TBCs occur within the TC just above

‡ Corresponding author
* Project (No. 2007CB707702) supported by the National Basic Research Program (973) of China

the thin TGO layer (Yamazaki *et al*., 2006), and with increasing TGO thickness, cracking was found to occur around interfacial defects and also within the TGO and along interfaces (Rabiei and Evans, 2000). To take full advantage of TBC systems, investigation and evaluation on the failure modes and delamination resistance of the TBC system are the important aspects to be undertaken.

A number of test methods have been developed to evaluate the adhesion and delamination toughness of the multilayered film/coating systems (e.g., TBCs), such as tensile tests (Qian *et al.*, 2003), four-point bending tests (Charalambides *et al.*, 1989; Hirakata *et al*., 2006; Yamazaki *et al*., 2006; Zhao *et al*., 2010), indentation tests (Dal Maschio *et al.*, 1994), scratch tests (Zaidi *et al*., 2006), double-cantilever beam tests (Li *et al.*, 2003), and blister tests (Zhou *et al*., 2002), etc. However, there are as yet no standard test methods to discover how to improve the reliability and durability of TBCs under severe thermal-mechanical loading conditions, which remains one of the major problems. Thus, the emphasis of the present work is to explore an experimental method that is easily carried out in an elevated temperature environment in laboratory, and would also yield a precise evaluation of delamination toughness in terms of the fracture mechanics concepts. From experimental analyses and theoretical calculations, fracture strength for crack initiation at the interfacial free edge and the delamination toughness of TBC systems can be derived.

2 Experimental

2.1 Materials and coating deposition methods

After being polished and sand-blasted, stainless steel SUS304 in a grooved rectangular shape with a thickness of 4.3 mm was used as the substrate. The nominal composition of the spray powder for the BC is Ni23Co20Cr8.5Al4Ta0.6Y (−37 μm, Armdry 997, Sulzer Metco Inc., New York, USA). Commercially available 8% (w/w) yttria-stabilized zirconia (8YSZ) powder ((−75+45) μm, Metco 204B-NS, Sulzer Metco Inc., New York, USA) was employed to prepare the YSZ TC.

An atmospheric plasma spraying (APS) system (80 kW class, GP-80, Jiujiang, China) was employed to deposit the BC and the YSZ TC. The approximate thickness of the deposited BC and 8YSZ coating were 100 and 250 μm, respectively. During plasma spraying, argon and hydrogen were used as the primary gas and the auxiliary gas, respectively. The pressures of both argon and hydrogen during spraying were maintained at 0.7 and 0.4 MPa, respectively. The flow rates of the primary and secondary gas were fixed at 60 and 3 L/min respectively to deposit the BC, likewise 60 and 5 L/min to deposit the YSZ TC. Nitrogen was used as the powder feeding gas operated at a pressure of 0.1 MPa and a flow rate of 0.25 L/min. Powder was fed externally to deposit the BC but fed internally to deposit the YSZ TC. The plasma jet was operated to deposit the BC at the power level of 30 kW (600 A, 50 V) with a spraying distance of 130 mm, and the YSZ TC was deposited at the power level of 39 kW (650 A, 60 V) with a spraying distance of 85 mm.

To prompt the delamination cracks to begin along TC/BC interface or within TC layer for TBC system, an experimental procedure of fabricating the special interface edge for crack initiation is briefly illustrated in Fig. 1. All the deposition processes included four steps. In step 1, the samples were ground and polished to 8 μm, and then corundum powder with 60 mesh grain size distribution was used for dry grit blasting. After this procedure, the substrates were coated with NiCoCrAlTaY powder. In step 2, partial surface of BC was tightly wrapped by a soft steel slice to expose the probable induced delamination area by test. Then the YSZ powder was sprayed on the surface in step 3. The covered soft slice was carefully removed from the BC and the desired asymmetric interface edge for crack initiation was formed, as shown in step 4. After deposition, the side view of specimen and the top coating surface were examined by scanning electron microscopy (SEM) (FEI-QUANTA 400, the Netherlands).

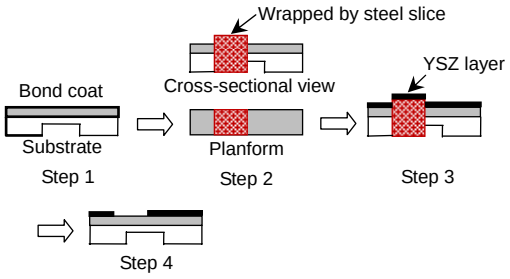

Fig. 1 Schematic diagram for creating interface edge

2.2 Modified three-point bending specimen preparation

At the beginning, two plates of stainless steel were polished with emery paper and diamond paste, and were cleaned by ultrasonic vibration in acetone and isopropyl alcohol. Then, the plates were glued with commercial adhesive (E-7, Shanghai Research Institute for Synthetic Resin, China) on the wafer with the TBC coatings. The curing of the adhesives was undertaken at 100 °C for 3 h. The wafer was cut into rectangular pieces by a dicing machine. Seven specimens were prepared and labeled TBC1–TBC7. The nominal dimensions of each specimen for the three-point bending test were 6 mm wide, 7.4 mm high and 42 mm long, and the substrate groove was 3 mm deep and 14 mm long; actual sizes of each specimen are given in Table 1. As shown in Fig. 2, the shape of each specimen is such that the bending moment nearby the loading point causes the delamination stress intensity near the interface edge.

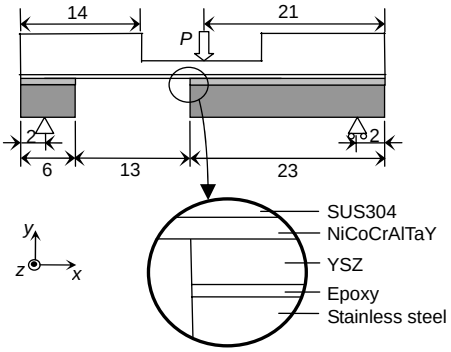

Fig. 2 Shape and size of the grooved modified three-point bending specimen (unit: mm)

2.3 Mechanical tests

Fig. 3 presents photographs showing the testing system and specimen. A monotonic load was applied to the specimen by a servo-hydraulic micro mechanical testing machine (Instron 5848 Microforce Tester, Canton, MA) equipped with a 2000 N load-cell. The tests were carried out under constant displacement rates 0.05–0.08 mm/min at the loading point, as shown in Table 1. All tests were conducted at a high ambient temperature of 100 °C, which was maintained by a temperature controller (Instron 3119 Environmental Chambers, Canton, MA), and held on for 15 min before load application. The load, P, and the loading point displacement, u, were continuously monitored during tests with a load-cell and a differential transformer, respectively. Loads were continually applied to let the crack initiation and propagation occur, and stopped when the crack tip crossed the loading point. Of the seven specimens tested, a total of four specimens were completed successfully. Fig. 4a shows the fracture process observed in the tests, and an enlarged view of crack region is shown in Fig. 4b. After testing, the specimens were fractured into two parts (i.e., one comprising the top substrate plate and the other the bottom stainless steel plate) and the microstructure of the fractured surfaces was analyzed using SEM imaging and energy disperse spectroscopy (EDS) detection.

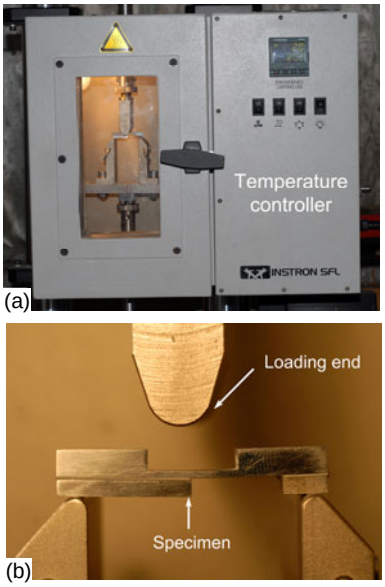

Fig. 3 Photographic illustration of testing system (a) and specimen (b)

Table 1 Specimen sizes and loading rates

Specimen No.	B (mm)	h_S (mm)	h_G (mm)	h_N (mm)	h_Y (mm)	h_E (mm)	h_B (mm)	Loading rate (mm/min)
TBC1	5.91	4.27	1.09	0.175	0.272	0.02	2.69	0.08
TBC2	5.96	4.30	0.99	0.146	0.278	0.03	2.68	0.08
TBC3	5.94	4.31	1.15	0.151	0.256	0.03	2.73	0.08
TBC4	5.97	4.28	1.04	0.143	0.251	0.02	2.73	0.05

B: specimen or crack width; h_S: thickness of substrate layer; h_G: thickness of grooved substrate region; h_N: thickness of bond coat layer; h_Y: thickness of 8YSZ ceramic layer; h_E: thickness of epoxy layer; h_B: thickness of bonded stainless steel layer

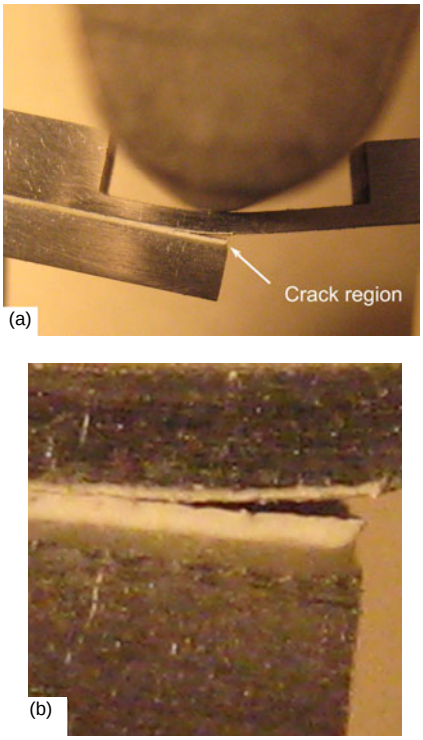

Fig. 4 Side views of specimen during the fracture process
(a) Overall view; (b) Enlarged view of crack region

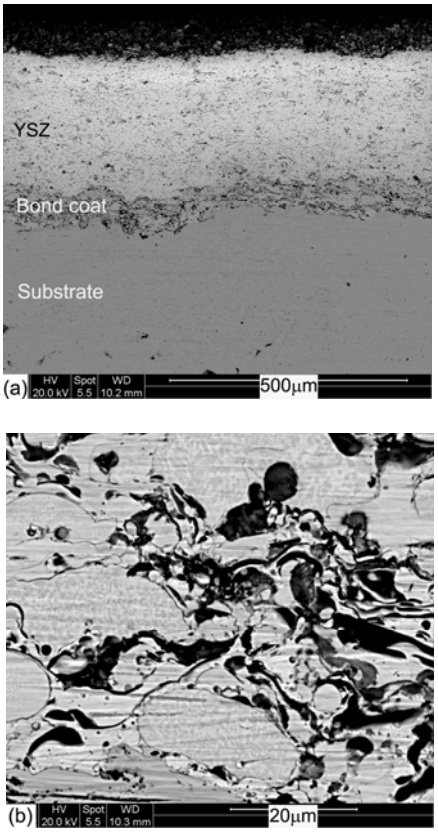

Fig. 5 Cross-sectional microstructure of the as-deposited TBC system
(a) Overall view; (b) Bond coat

3 Results and discussion

3.1 Microstructure of the as-deposited and fractured TBCs

Fig. 5a shows the cross-sectional SEM micrography of the as-deposited TBC system, which exhibits the substrate, BC and YSZ layers clearly. All coatings show a typical APS lamellar structure with inter-splat porosity, and the highly undulated nature of TC/BC interface, which are the characteristics of plasma-sprayed deposition. The roughness of TC/BC interface was increased with these interfacial undulations; therefore, the TC adhesion can be improved by mechanical keying. However, the ultimate failure of TBCs is primarily limited due to these undulations giving rise to out-of-plane tension. The BC exhibits a dense microstructure in comparison to the top coating, and no evident oxidation was observed during coating deposition, though some internal oxide stringers and pores induced by APS deposition are present in the BC (Fig. 5b).

Fig. 6a shows the typical surface morphology of particles impacting and stacking during plasma spraying. Examination of the fractured surfaces of the TBC specimens (Fig. 6b) demonstrated that most fracture surfaces exhibited a similar morphology (e.g., interspace, pores and microcracks) with that of the as-received TBC specimens (Fig. 6a). These differ only slightly in the bonded areas. This indicates that the cracks preferentially propagate along the interface area between lamellas in the coating where there existed a great number of nonbonded interfaces, according to (Ohmori and Li, 1991). Such crack propagation causes cohesive fracture that has been shown by McPherson and Shafer (1982). A closer examination of Fig. 6b revealed that the fractured surface presented terraced structural morphology. This suggests that cohesive cracking of the ceramic coating also occurs through trans-lamellae cracking by connecting those pre-existing vertical microcracks (Ohmori and Li, 1991).

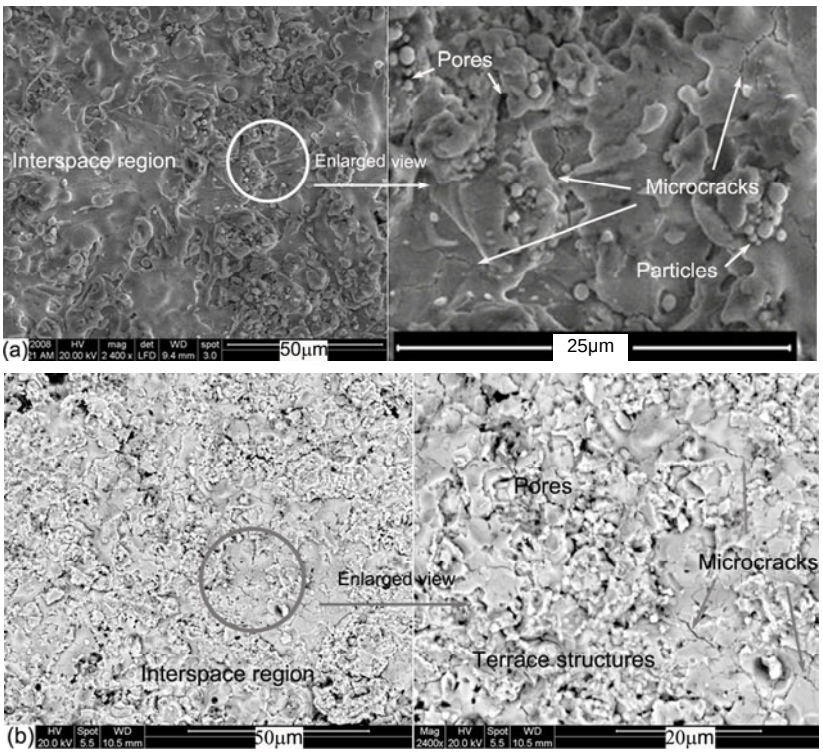

Fig. 6 Typical surface morphology of the YSZ coating

(a) As-received TBC specimens (the right figure is an enlarged view of the local region); (b) Fractured surfaces of TBC specimens (the right figure is an enlarged view of the local region)

3.2 Microstructural analysis of failure modes

Fig. 7 shows the SEM micrographs of subjacent fracture surfaces after mechanical testing. An overall view of surface morphology is shown in Fig. 7a, and the crack plane covered almost with uniform YSZ material is smooth. Fig. 7b illustrates a higher magnification image of the local region near the free edge in Fig. 7a (white casing area). This local view exhibits predominant YSZ material mingled with some BC constituent at edges, which is attributed to the undulated nature of TC/BC interface. Examinations of regions 1–3 on the lower fracture surfaces by EDS exhibited almost the same wave spectrum of high percentages of Zr and O, except for a little difference in atomic proportion. For avoiding repetition, a typical EDS spectrum from region 2 is shown in Fig. 8. Thus, the compositions of fracture surface are mainly YSZ material. All these figures indicate that delamination cracks initiated at the free edge of YSZ coating interlamellar in layer, and via interconnecting the transverse and vertical microcracks, cracks propagated stably along the extending direction within the TC, as shown in Fig. 7a. Repeated observations

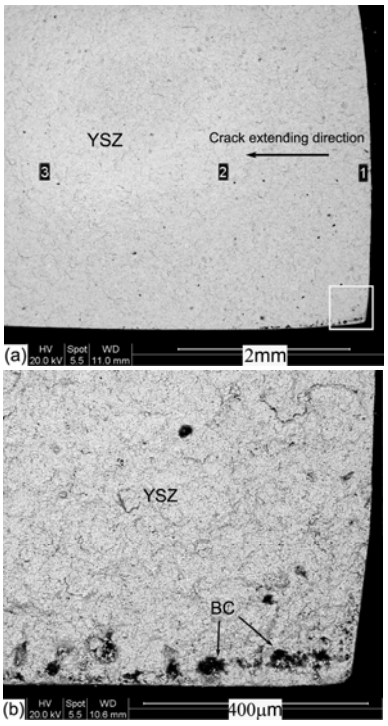

Fig. 7 Fracture topography of the fractured surfaces

(a) Subjacent coating surface; (b) Local region near the free edge

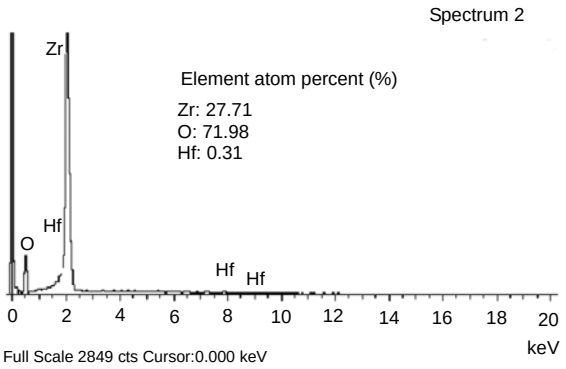

Fig. 8 EDS analysis from region 2 on the fractured surface in Fig. 7a

showed that failure modes in all tested TBC specimens are identical.

3.3 Testing results

As shown in Fig. 9, the curves of the load *P* against displacement *u* for all completed TBC specimens have similar shapes. With the increase of *u*, *P* initially increases linearly and climbs with some fluctuation, and then increases again proportionately. Take TBC3 for example, a schematic of these curves is given in Fig. 9a where the various stages are identified and various points labeled. As shown in Fig. 9a, over portion *AB* (1st stage), TBC specimens deformed linear elastically to accumulate strain energy for subsequent cracking. After the 1st stage, inter-splat delamination was observed to initiate at the free edge of YSZ layer when loads reach a certain critical value corresponding to one point near *B*. This edge crack was then rapidly developed to be one interfacial lamellar crack, corresponding to portion *BC* (2nd stage). Crack growth continues in a stable manner within the ceramic YSZ coating corresponding to portion *CD* (3rd stage). Therefore, it could be concluded that fracturing within modified three-point bending-TBC specimens comprises two stages, viz., stages 2 and 3, which is consistent with the microstructure analysis of fractured surfaces (Figs. 7 and 8).

4 Fracture strength of TBC coating

A 2D finite element model (FEM) was constructed to carry out a numerical analysis of all tested TBC specimens. Commercial FEM code ABAQUS 6.5 was used to implement the numerical analysis. Regions near the free edge of interface were carefully divided into fine meshes. Also, based on the geometric shape of specimens and loading conditions, elastic analyses were conducted for all specimens with displacement at the left supporting point fixed. Typical finite element mesh of specimen TBC3 is shown in Fig. 10. The elastic constants at 100 °C of each layer are shown in Table 2 (Pawlowski, 1995; Choi *et al*., 2004).

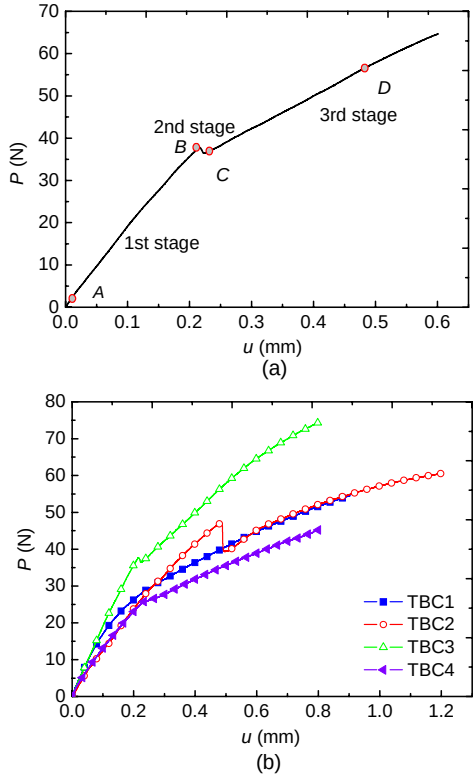

Fig. 9 Measured load-displacement relationships of the TBC specimens by mechanical tests
(a) Specimen TBC3; (b) All specimens

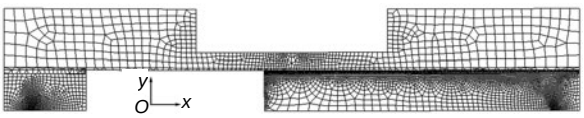

Fig. 10 Finite element mesh of specimen TBC3

Table 2 Elastic constants at 100 °C for finite element model analysis

Material	Young's modulus (GPa)	Poisson's ratio
SUS304	195	0.31
Epoxy	2.5	0.31
YSZ	15.5	0.04
NiCoCrAlTaY	160	0.30
Stainless steel	200	0.31

To investigate the fracture strength of TBC coatings, the stress distribution was calculated along the YSZ interfacial lamella for each TBC specimen at the moment of crack initiation. The distributions of both normal and shear stresses along this interface over the entire crack length are given in Fig. 11. It is shown that there exists a concentrated stress field near the free edges of interfacial lamellae, and the magnitudes of shear stress are comparable to those of normal stress. Numerical results reveal that peak normal stresses and peak shear stresses for crack initiation are about (68±20) and (−21±6) MPa, respectively. These are the interfacial tensile strength and shear strength that characterize the bonding strength which determines the material's resistance to crack initiation at the free edge of YSZ interfacial lamella.

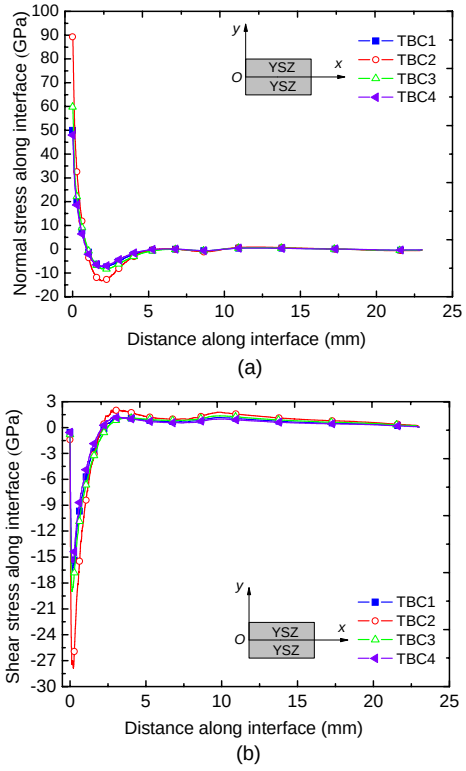

Fig. 11 Distributions of the normal stress (a) and shear stress (b) along the YSZ interfacial lamella at the instant of crack initiation

5 Delamination toughness

5.1 Analytical solutions

For the section of the crack located between the loading and supporting lines, the cracked ligament is subjected to constant moments. Consequently, the critical energy release rate G_c can be deduced analytically by recognizing that it is simply the difference in the strain energy between the uncracked and cracked sections. As shown in Fig. 12, we assume that a certain section near the YSZ layer edge stores the strain energy U_o before the crack arrives, and U_t when the new crack surface forms. Since the strain energy beneath the crack can be neglected, U_t can be derived from consideration of the strain energy in the uncracked section above the crack. As long as the crack extends uniformly within the TC layer, a bending moment M exists along the specimen cross section,

$$M = PL / B, \tag{1}$$

where P is the total load applied on specimen, L is the spacing between loading and supporting lines, and B is the specimen or crack width. From the Euler-Bernoulli beam theory and planar strain conditions, these strain energies can be expressed in terms of the applied moment M as

$$U = \frac{(1-\upsilon^2)M^2}{2EI}, \tag{2}$$

where $E=E'(1-\upsilon^2)$, E is Young's modulus, E' is equivalent modulus under plane strain condition, υ is Poisson's ratio, and I is the second moment of inertia of area per unit width. The material properties of each layer under planar stress state are shown in Table 2. Under the assumption of the generalized Hook law, the critical energy release rate can then be calculated as a modification of Charalambides *et al*. (1989),

$$G_c = U_t - U_o = \frac{M^2}{2}\left(\frac{1}{E'_{Ct}I_{Ct}} - \frac{1}{E'_{Co}I_{Co}}\right). \tag{3}$$

where E'_{Co} and I'_{Co} are the equivalent modulus and second moment of inertia of composite beam before the crack arrives, respectively. E'_{Ct} and I'_{Ct} are the equivalent modulus and second moment of inertia of composite beam after the new crack surface formation, respectively.

Since this three-point bending composite beam consists of multiple-layered materials, the following expressions are derived for the current coating system according to the mixture law for composite materials,

$$E'_{\mathrm{Co}} = E'_{\mathrm{S}}E'_{\mathrm{B}}E'_{\mathrm{E}}E'_{\mathrm{Y}}E'_{\mathrm{N}}(h_{\mathrm{G}}+h_{\mathrm{B}}+h_{\mathrm{E}}+h_{\mathrm{Y}}+h_{\mathrm{N}}) / (h_{\mathrm{B}}E'_{\mathrm{S}}E'_{\mathrm{B}}E'_{\mathrm{Y}}E'_{\mathrm{N}} + h_{\mathrm{E}}E'_{\mathrm{S}}E'_{\mathrm{B}}E'_{\mathrm{Y}}E'_{\mathrm{N}} + h_{\mathrm{Y}}E'_{\mathrm{S}}E'_{\mathrm{B}}E'_{\mathrm{E}}E'_{\mathrm{N}} + h_{\mathrm{N}}E'_{\mathrm{S}}E'_{\mathrm{B}}E'_{\mathrm{E}}E'_{\mathrm{Y}} + h_{\mathrm{G}}E'_{\mathrm{B}}E'_{\mathrm{E}}E'_{\mathrm{Y}}E'_{\mathrm{N}}), \tag{4}$$

$$E'_{\mathrm{Ct}} = \frac{E'_{\mathrm{S}}E'_{\mathrm{N}}E'_{\mathrm{Y}}(h_{\mathrm{G}}+h_{\mathrm{N}}+h'_{\mathrm{Y}})}{h_{\mathrm{G}}E'_{\mathrm{N}}E'_{\mathrm{Y}} + h_{\mathrm{N}}E'_{\mathrm{S}}E'_{\mathrm{Y}} + h'_{\mathrm{Y}}E'_{\mathrm{N}}E'_{\mathrm{S}}}, \tag{5}$$

where h_{S}, h_{G}, h_{N}, h_{Y}, h_{E}, and h_{B} is the thickness of substrate layer, grooved substrate region, BC layer, YSZ ceramic layer, epoxy layer, and bonded stainless steel layer, respectively. E'_{S}, E'_{G}, E'_{N}, E'_{Y}, E'_{E}, and E'_{B} is the equivalent modulus under plane strain condition of substrate layer, grooved substrate region, BC layer, YSZ ceramic layer, epoxy layer, and bonded stainless steel layer, respectively. The crack is assumed to grow along the middle thickness direction of the YSZ ceramic coating, i.e., $h'_{\mathrm{Y}}=h_{\mathrm{Y}}/2$ (Fig. 12).

Based on the curvature and axial force equations, the composite moments of inertia are as follows:

$$I_{\mathrm{Co}} = \frac{1}{3}\left((d+h_{\mathrm{N}}+h_{\mathrm{Y}}+h_{\mathrm{E}}+h_{\mathrm{G}})^3 + (h_{\mathrm{B}}-d)^3\right), \tag{6}$$

$$I_{\mathrm{Ct}} = \frac{1}{3}\left((d+h_{\mathrm{N}}+h_{\mathrm{Y}}+h_{\mathrm{E}}+h_{\mathrm{G}})^3 - \left(d+h_{\mathrm{E}}+\frac{1}{2}h_{\mathrm{Y}}\right)^3\right), \tag{7}$$

where d denotes the location of a neutral plane π, which is assumed to be identical within the uncracked and cracked sections (Fig. 12). Since the axial force on the neutral plane vanishes, $N=0$, d could be determined by

$$d = (2E'_{\mathrm{S}}h_{\mathrm{G}} + 2E'_{\mathrm{E}}h_{\mathrm{E}} + 2E'_{\mathrm{Y}}h_{\mathrm{Y}} + 2E'_{\mathrm{N}}h_{\mathrm{N}} + 2E'_{\mathrm{B}}h_{\mathrm{B}})^{-1} \times \{E'_{\mathrm{B}}h_{\mathrm{B}}^2 - E'_{\mathrm{E}}h_{\mathrm{E}}^2 - E'_{\mathrm{Y}}h_{\mathrm{Y}}^2 - E'_{\mathrm{N}}h_{\mathrm{N}}^2 - E'_{\mathrm{S}}h_{\mathrm{G}}^2 - 2[E'_{\mathrm{Y}}h_{\mathrm{Y}}h_{\mathrm{E}} + E'_{\mathrm{N}}h_{\mathrm{N}}(h_{\mathrm{Y}}+h_{\mathrm{E}}) + E'_{\mathrm{S}}h_{\mathrm{G}}(h_{\mathrm{E}}+h_{\mathrm{Y}}+h_{\mathrm{N}})]\}. \tag{8}$$

Using Eqs. (3)–(7), G_{c} can therefore be derived by determining the critical fracture load P_{c} from the load-displacement curve of the specimen.

5.2 Discussion

Variations of energy release rate with applied loads for all TBC specimens tested are represented in Fig. 13. Due to the assumptions made in obtaining the analytic solution, values of fracture toughness for cracks of smaller lengths are in close agreement with actual materials property. Calculated energy release rates G at the corresponding critical fracture loads are shown in Table 3. From these results, we conclude that the fracture toughness of the ceramic 8YSZ coating at 100 °C is approximately 5–15 J/m^2, in terms of the energy release rate. Most of studies reported the fracture toughness of ceramic YSZ coating at room temperature. For example, Rabiei and Evans (2000) implemented indentation tests and obtained a fracture toughness of about 10–49 J/m^2 (we calculated from the measured values of K_{Ic}=0.7 MPa·m$^{0.5}$, E_{TBC}= 10–50 GPa for plasma-sprayed YSZ coatings). Choi *et al.* (2004) utilized both the single edge V-notched beam and the double-cantilever beam methods, and an averaged fracture toughness of about 44 J/m^2 was estimated for free-standing APS-TBC coating. Zhao *et al.* (2010) reported a mean fracture toughness of 17–35 J/m^2 for plasma-sprayed 8YSZ coating, which were determined by adopting a modified four-point bending specimen. The critical energy release rates obtained from this study compare reasonably well to those obtained by other researches.

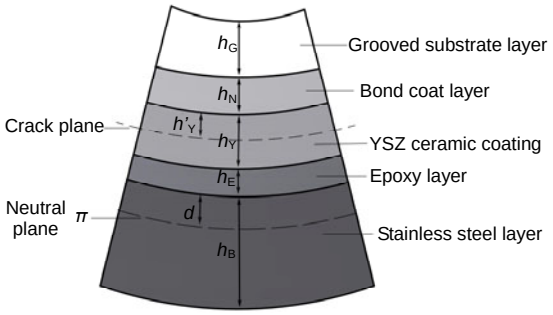

Fig. 12 Multiple-layered section of the cracked segment on specimen

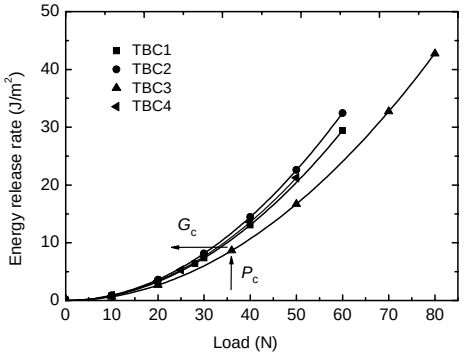

Fig. 13 Variations of energy release rate with applied load during three-point bending tests

Table 3 Critical energy release rate of TBC specimens

Specimen No.	P_c (N)	G_c (J/m^2)
TBC1	28	6.4
TBC2	40	14.5
TBC3	36	8.7
TBC4	25	5.3

P_c: critical fracture load; G_c: energy release rate at the corresponding critical fracture load

It is worth to discuss that TBCs' microstructure and test method could be the main factors that result in the difference in measured strain energy release for APS ZrO_2-Y_2O_3 coatings. The tested materials were all composed of the standard constituent (7%–8% (w/w) YSZ); however, the coating process and spray parameters might be different, which caused TBCs' microstructure to be various. Therefore, the orientation, dimensions, shape, distribution of microcracks and pores, and the interspace level should be responsible for the difference in the measurement of fracture toughness. Moreover, different specimen types and test methods might generate different results.

6 Conclusions

The failure mode and adhesion of TBCs 8YSZ deposited on NiCoCrAlTaY BC by the APS method were investigated experimentally. A grooved modified three-point bending specimen that generates only a single interface crack was adopted in tests. The load-displacement curves combining microstructural examinations showed that delamination cracks initiated at the free edge of YSZ coating interlamellar, propagated stably within top coating. Finite element analyses were performed to extract the interfacial tensile strength and shear strength for crack initiation at the free edge of YSZ interfacial lamellae, and their calculated values were approximately (68±20) and (–21±6) MPa, respectively. The delamination toughness of ceramic 8YSZ coating at 100 °C was measured to be approximately 5–15 J/m^2, determined from analytical considerations. These measurement values are a bit lower than those of similar ceramic coatings at room temperature, typically 17–35 J/m^2 for plasma-sprayed 8YSZ coatings. This suggests the necessity of exploring the fracture toughness of a TBC coating system at elevated temperatures.

Acknowledgements

The authors would like to thank Profs. Chang-jiu LI, Guan-jun YANG, and Dr. Yong LI from School of Materials Science and Engineering, Xi'an Jiaotong University, China for providing the TBC materials and many helpful suggestions.

References

Brindley, W.J., 1996. Thermal barrier coatings. *Journal of Thermal Spray Technology*, **5**(4):379-380. [doi:10.1007/BF02645266]

Charalambides, P.G., Lund, J., Evans, A.G., 1989. A test specimen for determining the fracture resistance of bimaterial interfaces. *Journal of Applied Mechanics*, **56**:77-82. [doi:10.1115/1.3176069]

Choi, S.R., Zhu, D., Miller, R.A., 2004. Mechanical properties/database of plasma-sprayed ZrO_2-8% (w/w) Y_2O_3 thermal barrier coatings. *International Journal of Applied Ceramic Technology*, **1**(4):330-342. [doi:10.1111/j.1744-7402.2004.tb00184.x]

Dal Maschio, R., Sgiavo, V.M., Mattivi, L., Bertamini, L., Sturlese, S., 1994. Indentation method for fracture resistance determination of metal/ceramic interfaces in thick TBCs. *Journal of Thermal Spray Technology*, **3**(1):51-56. [doi:10.1007/BF02648999]

Evans, A.G., Mumm, D.R., Hutchinson, J.W., Meier, G.H., Pettit, F.S., 2001. Mechanisms controlling the durability of thermal barrier coatings. *Progress in Materials Science*, **46**(5):505-553. [doi:10.1016/S0079-6425(00)00020-7]

Hirakata, H., Kitazawa, M., Kitamura, T., 2006. Fatigue crack growth along interface between metal and ceramics submicron-thick films in inert environment. *Acta Materialia*, **54**(1):89-97. [doi:10.1016/j.actamat.2005.08.026]

Li, C.J., Wang, W.Z., He, Y., 2003. Measurement of fracture toughness of plasma-sprayed Al_2O_3 coatings using a tapered double cantilever beam method. *Journal of the American Ceramic Society*, **86**(8):1437-1439. [doi:10.1111/j.1151-2916.2003.tb03491.x]

McPherson, R., Shafer, B.V., 1982. Interlamellar contact within plasma-sprayed coatings. *Thin Solid Films*, **97**(3):201-204. [doi:10.1016/0040-6090(82)90453-9]

Miller, R.A., 1987. Current status of thermal barrier coatings—an overview. *Surface and Coatings Technology*, **30**(1):1-11. [doi:10.1016/0257-8972(87)90003-X]

Miller, R.A., 1997. Thermal barrier coatings for aircraft engines: history and directions. *Journal of Thermal Spray Technology*, **6**(1):35-42. [doi:10.1007/BF02646310]

Ohmori, A., Li, C.J., 1991. Quantitative characterization of the structure of plasma-sprayed Al_2O_3 coating by using copper electroplating. *Thin Solid Films*, **201**(2):241-252. [doi:10.1016/0040-6090(91)90114-D]

Pawlowski, L., 1995. The Science and Engineering of Thermal Spray Coatings. Chichester, Wiley Press, New York, USA.

Qian, L., Zhu, S., Kagawa, Y., Kubo, T., 2003. Tensile damage evolution behavior in plasma-sprayed thermal barrier coating system. *Surface and Coatings Technology*, **173**(2-3):178-184. [doi:10.1016/S0257-8972(03)00429-8]

Rabiei, A., Evans, A.G., 2000. Failure mechanisms associated with the thermally grown oxide in plasma-sprayed thermal barrier coatings. *Acta Materialia*, **48**(15):3963-3976. [doi:10.1016/S1359-6454(00)00171-3]

Yamazaki, Y., Schimdt, A., Scholz, A., 2006. The determination of the delamination resistance in thermal barrier coating system by four-point bending tests. *Surface and Coatings Technology*, **201**(3-4):744-754. [doi:10.1016/j.surfcoat.2005.12.023]

Zaidi, H., Djamai, A., Chin, K.J., Mathia, T., 2006. Characterisation of DLC coating adherence by scratch testing. *Tribology International*, **39**(2):124-128. [doi:10.1016/j.triboint.2005.04.016]

Zhao, P.F., Sun, C.A., Zhu, X.Y., Shang, F.L., Li, C.J., 2010. Fracture toughness measurements of plasma-sprayed thermal barrier coatings using a modified four-point bending method. *Surface and Coatings Technology*, **204**(24):4066-4074. [doi:10.1016/j.surfcoat.2010.05.029]

Zhou, Y.C., Hashida, T., Jian, Y.C., 2002. Determination of interface fracture toughness in thermal barrier coating system by blister test. *Journal of Engineering Materials and Technology*, **125**(2):176-182. [doi:10.1115/1.1555658]